日本磁気学会
ISSN 2432-0250
Journal of the Magnetics Society of Japan
Electronic Journal URL: https://www.jstage.jst.go.jp/browse/msjmag

Vol.45 No.5 2021

Journal

Review: MSJ Awards 2020

Crystal Structure and Magnetic and Magneto-optical Properties of CoPt, $MnPt_3$, $CrPt_3$, MnAl and MnGa Films with Ordered Phase and Their Bit-patterned Media

S. Iwata, T. Kato, and D. Oshima …118

Power Magnetics

Reluctance Network Model of Interior Permanent Magnet Motor with Polar Anisotropic Magnet

Y. Hane, Y. Uchiyama, and K. Nakamura …125

Biomagnetism / Medical Applications

Magnetocardiography Current Source Estimation using Multiple Spatial Filters

K. Kobayashi, M. Iwai, Y. Ono, W. Sun, M. Sugimachi, K. Kusano, and T. Shishido …131

JOURNAL OF THE MAGNETICS SOCIETY OF JAPAN

Vol.45 No.5 2021

日本磁気学会

ISSN 2432-0250

HP: http://www.magnetics.jp/ e-mail: msj@bj.wakwak.com

Electronic Journal: http://www.jstage.jst.go.jp/browse/msjmag

Journal of the Magnetics Society of Japan
Vol. 45, No. 5

Electronic Journal URL: https://www.jstage.jst.go.jp/browse/msjmag

CONTENTS

Review: MSJ Awards 2020

Crystal Structure and Magnetic and Magneto-optical Properties of CoPt, $MnPt_3$, $CrPt_3$, MnAl and MnGa Films with Ordered Phase and Their Bit-patterned Media
..... S. Iwata, T. Kato, and D. Oshima 118

Power Magnetics

Reluctance Network Model of Interior Permanent Magnet Motor with Polar Anisotropic Magnet
..... Y. Hane, Y. Uchiyama, and K. Nakamura 125

Biomagnetism / Medical Applications

Magnetocardiography Current Source Estimation using Multiple Spatial Filters
..... K. Kobayashi, M. Iwai, Y. Ono, W. Sun, M. Sugimachi, K. Kusano, and T. Shishido 131

J. Magn. Soc. Jpn., **45**, 118-124 (2021)

<Review>

Crystal Structure and Magnetic and Magneto-optical Properties of CoPt, $MnPt_3$, $CrPt_3$, MnAl and MnGa Films with Ordered Phase and Their Bit-patterned Media

S. Iwata, T. Kato*, and D. Oshima*

Nagoya Industrial Science Research Institute, *Yotsuyadori 1-13, Chikusa-ku, Nagoya 464-0819, Japan*

*Institute of Materials and Systems for Sustainability, Nagoya Univ., *Furo-cho, Chikusa-ku, Nagoya 464-8603, Japan*

This paper reviews the crystal structure and magnetic and magneto-optical properties of CoPt, $MnPt_3$, $CrPt_3$, MnAl and MnGa films with an ordered phase as well as dot patterns fabricated on these films. CoPt film grown on a MgO (111) substrate at 300˚C had an $L1_1$ phase and exhibited a large perpendicular anisotropy. $CrPt_3$ films, which had a (111) orientation and $L1_2$ phase, showed a large perpendicular anisotropy due to the magneto-elastic effect. By utilizing the change from $L1_2$ to a disordered phase caused by low-dose Kr^+ ion irradiation, dot patterns were prepared on $CrPt_3$ film with a flat surface. It was found that a CoGa buffer layer was effective at growing thinner $L1_0$ MnAl and MnGa films on a MgO (001) substrate while keeping a (001) orientation. In the case of fabricating MnGa on SiO_2/Si substrates, a buffer layer of CoGa/Cr/MgO/Cr/NiTa was necessary to grow $L1_0$ MnGa with a (001) orientation.

Key words: ordered alloy film, perpendicular anisotropy, magneto-elastic effect, magneto-optical effect, ion irradiation, bit-patterned media

1. Introduction

The study on crystal structure, magnetic properties and bit pattern fabrication of various ordered alloy films are introduced in this review paper, which is a research subject related to MSJ Achievement Award 2020. Multilayers and ordered alloy films of 3d-transition metals and noble metals were intensely studied from late 1980s as potential materials for magneto-optical and perpendicular magnetic recording because of their large perpendicular magnetic anisotropy and magneto-optical effect. After commercialization of magneto-optical recording in late 1980s using TbFeCo amorphous alloy films, Co/Pt and Co/Pd multilayers were received much attention as next generation materials for high density magneto-optical recording using a blue laser due to their large magneto-optical Kerr rotation around 300 nm[1)-3)]. Ordered CoPt and FePt alloy films with $L1_0$ structure were successively investigated because they exhibit larger perpendicular anisotropy and magneto-optical effect than multilayers[4)-6)].

In addition, perpendicular anisotropy was reported in CoPt film with non-equilibrium $L1_1$ phase[7)-9)] and $CrPt_3$ film with $L1_2$ phase[10), 11)]. Magnetic properties of $CrPt_3$ films can be controlled from ferrimagnetic to non-magnetic by ion irradiation since ion-implantation destroys ordered $L1_2$ phase and alters magnetism to non-magnetic phase. Utilizing resist patterning and ion irradiation, bit patterns of perpendicular magnetized $CrPt_3$ films can be fabricated without etching process of the film[12)-14)]. After 2010s, perpendicular magnetized MnAl and MnGa films with $L1_0$ phase were received a lot of attention as spintronic materials because of their high spin polarization and low Gilbert damping[15)-18)]. They are also useful materials for bit pattern processing by ion irradiation[19), 20)].

Corresponding author: S. Iwata (e-mail: fujitsuka_iwata@yahoo.co.jp).

2. $L1_1$ CoPt films grown on MgO (111)

Two ordered phases of $L1_0$ CoPt and $L1_2$ $CoPt_3$ can be seen in phase diagram of Co-Pt binary alloy. $L1_0$ CoPt with tetragonal lattice has the structure that atomic mono-layers of Co and Pt stacked in [001] direction and (001) oriented CoPt film exhibits a large perpendicular anisotropy of 5×10^7 erg/cc[21)]. On the other hand, $L1_2$ $CoPt_3$ film does not show uniaxial anisotropy due to its cubic lattice. In case of film fabrication by vapor or sputtering deposition, non-equilibrium structure which is not seen in phase diagram was sporadically appeared under specific growth conditions. Authors reported that $Co_{50}Pt_{50}$ films MBE-grown on a single crystal MgO(111) substrate show very large perpendicular anisotropy[7)]. Since the $L1_0$ CoPt film with (111) orientation does definitely not show perpendicular anisotropy, formation of an unknown phase was presumed. Figure 1 shows X-ray diffraction patterns of Pt(2 nm)/$Co_{50}Pt_{50}$(100 nm)/Pt(10 nm)/Ag(40 nm)/MgO (001) and Pt(2 nm)/$Co_{50}Pt_{50}$(100 nm)/MgO(111) films[7)]. In case of the CoPt film grown on MgO(001) at 300˚C, superlattice line due to $L1_0$ phase is observed in 2θ=24˚. In case of the film on MgO(111) grown at 200˚C and 300˚C, a strong peaks around 2θ = 20˚ and 65˚ are seen. This implies that a superlattice in the film normal direction is formed. In order to identify crystal structure of this film, the reciprocal space map was measured along the Q_z and Q_x axes as shown in Fig. 2 (a), where Q_z is perpendicular component of the momentum transfer vector and Q_x the in-plane component of [11-2] direction.

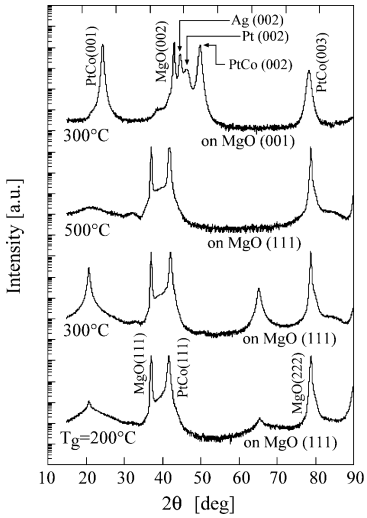

Fig. 1 X-ray diffraction patterns of $Pt_{50}Co_{50}$ (100 nm) films grown on (111) and (001) MgO substrates with various growth temperatures.

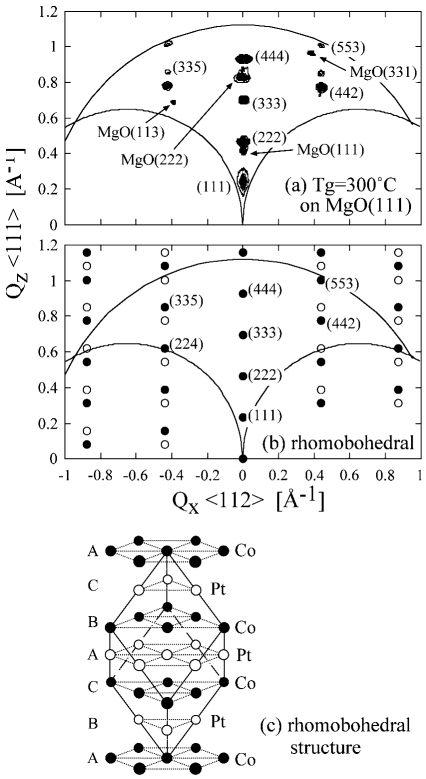

Fig. 2 Reciprocal space maps for (a) $Pt_{50}Co_{50}$ film grown on MgO (111) at 300˚C and (b) twinned rhombohedral system, where closed and open circles indicate diffraction spots from ABC and ACB stacking, respectively. Lattice image of rhombohedral system (c).

Figure 2 (b) illustrates the predicted map for the rhombohedral lattice shown in Fig. 2 (c), where close packed (111) planes of Co and Pt mono-layers alternately stack and a twinned structure composed of ABC and ACB stacking is formed. The experimental map of the CoPt film well coincides with the predicted map of the rhombohedral lattice. Although the rhombohedral phase called as $L1_1$ does not appear in the Co-Pt phase diagram, it is seen in Cu-Pt diagram. Figure 3 shows the dependence of perpendicular anisotropy on the growth temperature. The $L1_1$ CoPt film grown at 300˚C exhibits large anisotropy of 1.7×10^7 erg/cc, which is approximately same value with $L1_0$ CoPt film with (001) orientation. The CoPt film on MgO(111) at 500˚C does not show perpendicular anisotropy because of formation of $L1_0$ phase instead of $L1_1$. The preparation of perpendicular magnetized $L1_1$ CoPt films by sputtering was also reported by H. Sato *et al.*[22)]

Figure 4 shows the spectra of magneto-optical Kerr rotation θ_k for the $L1_1$ film at 300˚C, the $L1_0$ film at 300˚C and other magneto-optical materials[7), 10), 23)-26)]. The difference in θ_k spectra between $L1_1$ and $L1_0$ CoPt films may reflect the difference in coordination number of Co and Pt atoms.

3. $L1_2$ $MnPt_3$ and $CrPt_3$ films grown on fused quartz

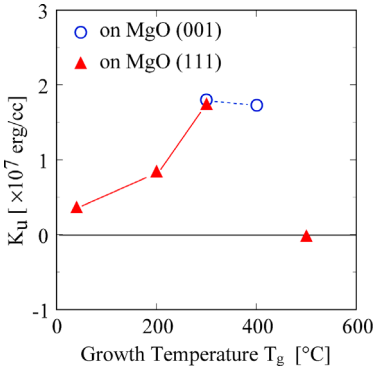

Fig. 3 Growth temperature T_g dependence of perpendicular anisotropy K_u for $Pt_{50}Co_{50}$ (100 nm) films.

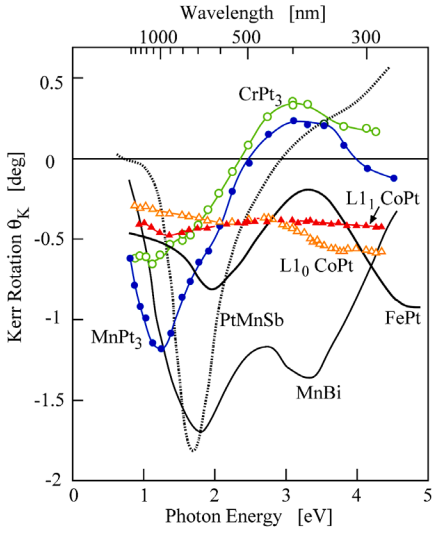

Fig. 4 Spectra of Kerr rotation θ_K for various magneto-optical materials.

Alloys containing Mn such as MnBi and PtMnSb are known as materials that exhibit large magneto-optical effect[23), 25)]. It was found that $MnPt_3$ and $CrPt_3$ films with $L1_2$ phase also show a large Kerr rotation as shown in Fig. 4[10), 26), 27)]. $MnPt_3$ and $CrPt_3$ films were prepared by sputtering on a fused quartz substrate and post-annealed at 800°C. Their phase was confirmed to be $L1_2$ by X-ray diffraction. $MnPt_3$ film shows a large Kerr rotation of 1.2° at 1.2 eV, which is larger than those for CoPt and FePt films. While the Kerr rotation of $CrPt_3$ film is smaller than that of $MnPt_3$ in energy range from 0.8 eV to 2.3 eV, the shape of Kerr spectrum of $CrPt_3$ is similar to that for $MnPt_3$. Figure 5 shows the hysteresis loops for the $MnPt_3$ and $CrPt_3$ films[28), 29)]. The $MnPt_3$ film is in-plane magnetized but the $CrPt_3$ perpendicular magnetized. Since the crystal structure of $L1_2$ $CrPt_3$ is a cubic lattice, the perpendicular anisotropy could not be induced from crystal anisotropy. In order to identify the origin of the anisotropy of the $CrPt_3$ film, the relationship between the perpendicular anisotropy K_u and the lattice distortion was measured as shown in Fig. 6[11)]. The distortion was defined as $2(a_i-a_p)/(2a_i+a_p)$, where a_i and a_p were in-plane and normal lattice constants, respectively. The $CrPt_3$ film on a fused quartz, which shows a large anisotropy, is distorted by 0.7 %. This is because that the film is expanded in in-plane direction due to the difference of thermal expansion coefficient between the film and the quartz substrate during a cooling process after annealing. On the other hand, the $CrPt_3$ film on a MgO(111)

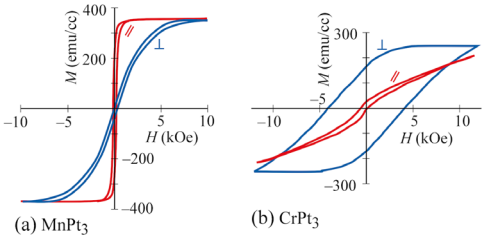

Fig. 5 *M-H* loops of $MnPt_3$ (150 nm) and $CrPt_3$ (150 nm) films with $L1_2$ phase.

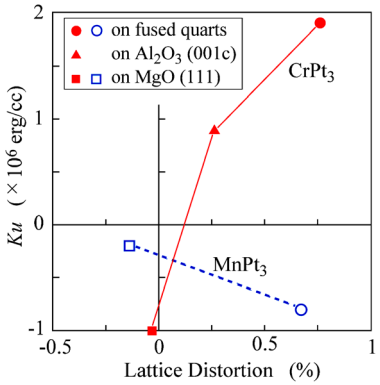

Fig. 6 Dependence of uniaxial anisotropy K_u on lattice distortion for $CrPt_3$ (60 nm) and $MnPt_3$ (60 nm) alloy films grown on fused quartz, MgO (111) and Al_2O_3 (001c).

Table 1 Magneto-striction constants λ_{100} and λ_{111} of MBE-grown $CrPt_3$ and $MnPt_3$ films on fused quartz.

	λ_{100}	λ_{111}
$MnPt_3$	5×10^{-5}	3×10^{-5}
$CrPt_3$	-16×10^{-5}	-4×10^{-5}

substrate, which does not show perpendicular anisotropy, is not distorted because the thermal expansion coefficient of MgO is almost same as that for the $CrPt_3$ film. This difference between the films on fused quartz and MgO implies that the anisotropy of $CrPt_3$ films is affected from magneto-elastic effect. The magneto-striction constants shown in Table 1 were estimated from the variation of anisotropy by bending the film on fused quartz of 0.1 mm thickness[11)]. The magneto-striction constants λ_{100} and λ_{111} of $CrPt_3$ are both negative while those of $MnPt_3$ are positive. Using the value of lattice distortion and the magneto-striction constants, the magneto-elastic contribution to perpendicular anisotropy were estimated as 1.4×10^6 erg/cc for $CrPt_3$ film and -0.9×10^6 erg/cc for $MnPt_3$ film on fused quartz, which are comparable to the measured anisotropy shown in Fig. 6. This means that the origin of the perpendicular anisotropy of $CrPt_3$ on fused quartz is magneto-elastic effect.

Since the $CrPt_3$ films is ferrimagnetic and perpendicular magnetized in $L1_2$ phase and non-magnetic in disordered phase, the fabrication of patterned media was made by phase transition using ion irradiation on $L1_2$ $CrPt_3$ films[30)]. Figure 7 shows the reduction of anisotropy K_u and magnetization M_s by Kr^+ ion irradiation of 30 kV to $L1_2$ $CrPt_3$ film with 20 nm thickness[12), 13)]. The K_u and M_s monotonically decrease with ion dose and are reduced to almost zero at 2×10^{14} ions/cm^2, which implies that the crystal structure is transformed to disordered phase. Figure 8 shows MFM image of bit patterned $CrPt_3$ film, which was fabricated by the formation of resist patterns on $CrPt_3$(20 nm) film and the iron irradiation of 2×10^{14} ions/cm^2. The MFM

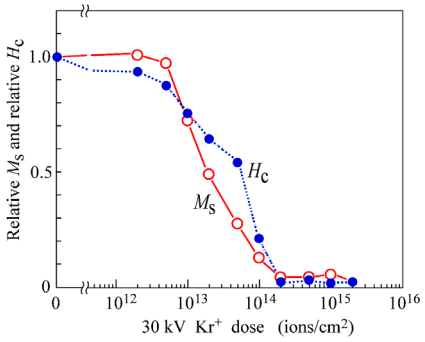

Fig. 7 Dependence of normalized saturation magnetization M_s and coercivity H_c of $CrPt_3$ (20 nm) on 30 kV Kr^+ ion dose.

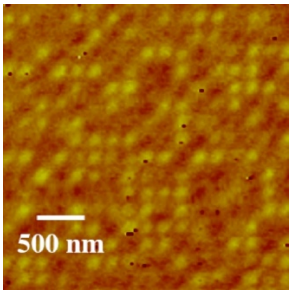

Fig. 8 MFM image of ion-beam-patterned $CrPt_3$ (20 nm) film with square bit size of 90×90 nm^2 separated by spacing of 90 nm fabricated with 30 keV Kr^+ irradiation of 2×10^{14} ions/cm^2 through ZEP resist mask made by EB lithography.

image shows that the square bit patterns of 90×90 nm^2 are formed and are randomly magnetized. It is considered to be effective to obtain bit patterned media with very flat surface by utilizing the transition from magnetic to non-magnetic states in ordered alloy films.

4. $L1_0$ MnAl and MnGa films grown on MgO (001)

In previous section, it is presented that bit patterned media can be fabricated utilizing phase change of perpendicular magnetized $L1_2$ $CrPt_3$ films. However, the practical application of $CrPt_3$ to magnetic recording media is not easy because of the high preparation temperature around 800°C. In the next step, $L1_0$ MnAl and MnGa films were investigated because these films exhibit larger perpendicular anisotropy than $CrPt_3$ film and can be fabricated at a relatively low process temperature around 400°C[31), 32)]. In addition, these materials are promising candidates for a ferromagnetic electrode of spintronic devices due to their low Gilbert damping.

In the first place, using single crystal MgO(001) substrates, Cr(2 nm)/(MnAl or MnGa)(15 nm)/Cr(20 nm) /MgO(001) films were fabricated by sputtering, where the Cr buffer layer was annealed at 600°C after deposition at room temperature, the MnAl layer was grown at 600°C and the MnGa layer was annealed 30 minutes at 400°C after deposition at less than 100°C. While the both MnAl and MnGa films show large perpendicular anisotropy as shown in Fig. 9, the squareness of the MnGa film is better

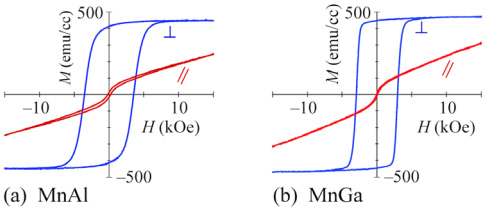

Fig. 9 *M-H* loops of (a) MnAl (15 nm) and (b) MnGa (15nm) films with $L1_0$ phase grown on MgO (001) substrates.

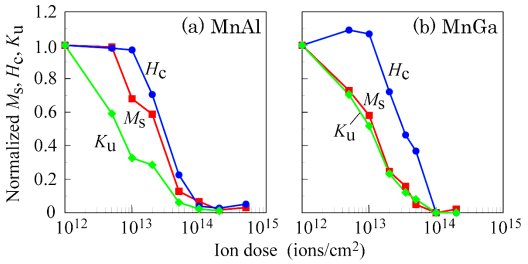

Fig. 10 30 keV Kr^+ ion dose dependence of normalized M_s, H_c, and K_u of (a) MnAl (15 nm) and (b) MnGa (15 nm) films.

than that of the MnAl film[20), 33)]. In addition, the saturation magnetization and squareness of MnAl films decline with decreasing growth temperature to 500°C.

Figure 10 shows the dependence of magnetization M_s, perpendicular anisotropy K_u and coercivity H_c on ion dose of 30 keV Kr^+, where these values are normalized as the values before ion irradiation[20), 33)]. The M_s, K_u and H_c are reduced to nearly zero at 1×10^{14} ions/cm^2, which is almost same as that for $CrPt_3$ film shown in Fig. 7. The K_u of MnGa film proportionally decreases with M_s, whereas the K_u of MnAl decreases faster than the M_s. In case of MnGa film, the H_c temporarily increases by 10 % and then steeply decreases with the ion dose. This increase of H_c is considered due to the creation of pinning sites by ion irradiation. The reason of these difference between MnGa and MnAl films is considered to be island growth of MnAl films grown at 600°C and smaller average mass of MnAl, which causes straightforward penetration of ions compared to MnGa.

Figure 11 shows MFM images of bit patterns of MnGa film fabricated by ion dose of 1×10^{14} ions/cm^2 [19), 20)]. The clear magnetic contrast due to randomly magnetized bits is observed in both pitch sizes of 100 and 80 nm. In order to fabricate smaller bit patterns than 80 nm, it is necessary to decrease the thickness of MnGa layer, because sharper transition interface between magnetic and non-magnetic areas will be realized by shortening the penetration depth of ion irradiation and suppressing ion scattering in MnGa layer. However, the M_s and the squareness of both MnAl and MnGa decrease with decreasing layer thickness from 15 nm to 5 nm[34)]. Since it had been reported that the insertion of CoGa buffer

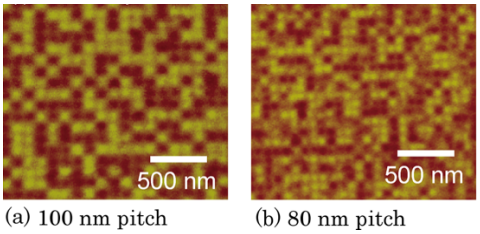

Fig. 11 MFM images of ion-beam patterned MnGa (15 nm) film with pitch sizes of (a) 100 nm and (b) 80 nm.

layer was effective to improve the degradation of M_s and squareness[35), 36)], Cr(2 nm)/MnAl(5 nm)/CoGa(0 or 30 nm) /Cr(20 nm)/MgO(001) films were fabricated by sputtering, where the CoGa/Cr layers were annealed at 600˚C after deposition at 400˚C and the MnAl layer was deposited at 200˚C. Figure 12 shows XRD profiles of 5nm thick MnAl films on Cr or CoGa buffer layer, where one of MnAl film on CoGa layer was post-annealed at T_a=500˚C and another was not annealed[34)]. The 001 and 002 peaks from $L1_0$ MnAl were clearly observed in all films and both the insertion of the CoGa buffer layer and the post-annealing of the MnAl layer are effective to enhance 001 peak due to the ordered phase. The peak positions of 001 and 002 are shifted to high angle side from the angles for bulk $L1_0$ MnAl, which are indicated by dotted lines in Fig. 12. This is because the lattice constant of MnAl layer is enlarged in in-plane direction due to lattice mismatch between MnAl and the buffer CoGa or Cr layers. Figure 13 shows the hysteresis loops of these films[34)]. The M_s of the MnAl (5 nm) on Cr layer significantly decreases compared to the MnAl (15 nm) film shown in Fig. 9, whereas the M_s and squareness of the MnAl (5 nm) on CoGa are considerably improved.

5. $L1_0$ MnGa films grown on Si

In order to utilized MnAl or MnGa films as magnetic recording media, (001) oriented films with $L1_0$ phase must be grown on inexpensive substrates instead of single crystal MgO substrates. Successively, (001) oriented MnGa film was made an attempt to be grown on Si substrate with SiO_2 oxidized layer. Since it had been reported that the insertion of CrB/NiTa buffer layer improved (001) orientation of $L1_0$ FePt films[37)], Cr(5 nm)/MnGa(15 nm)/Cr(20 nm)/MgO(5 nm)/CrB(5 nm)/NiTa(25 nm)/SiO2/Si substrate films were fabricated, where CrB/NiTa and Cr/MgO layers were grown by sputtering and e-beam evaporation at room temperature, respectively and then annealed at 800˚C[38)]. The MnGa layer was annealed at 400˚C for 60 minutes after sputter deposition at temperature T_s. Figure 14 shows XRD profiles of MnGa films on Si substrate grown at various T_s. The 002 peaks of MgO and Cr layers are clearly observed in all films, which means that the buffer layers are grown with (001) orientation. In addition, the 001 peak from $L1_0$ MnGa phase was observed for the films of T_s=200 and 300˚C, whose 001 peak position coincides with the bulk position indicated by a dotted line. Both M_s and squareness of out-of-plane M-H loops are improved by raising the growth temperature at T_s=200˚C as shown in Fig. 15. Figure 16 shows the MFM images of the dot-patterned MnGa film with 300, 150 and 100 nm pitch sizes fabricated by the 30 keV Kr^+ ion dose of 1×10^{14} ions/cm^2. Although the magnetic dot images are observed in all the samples, the outlines of circular dots is not sharp and some of dots do not show clear magnetic contrast. This implies that the improvement of

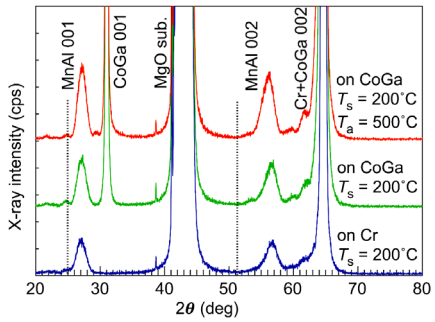

Fig. 12 XRD profiles of MnAl (5 nm) films grown on Cr and CoGa layers at T_s = 200˚C, where profiles are shown in linear scale. One sample on CoGa was post-annealed at 500˚C and another was not annealed. Dotted lines indicate peak positions of bulk $L1_0$-MnAl.

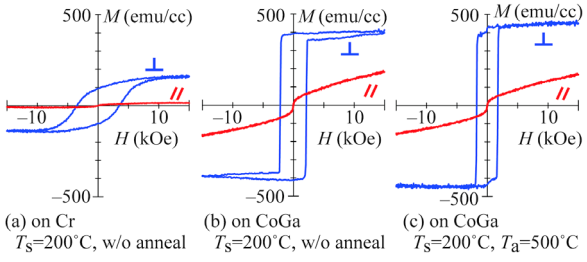

Fig. 13 M-H curves of MnAl (5 nm) films grown on (a) Cr and (b), (c) CoGa layers at T_s = 200˚C. Sample (c) was post-annealed at T_a = 500˚C.

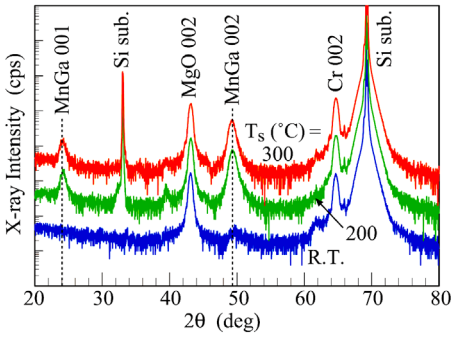

Fig. 14 X-ray profiles of MnGa (15 nm) films on Si substrate grown at various temperatures T_s.

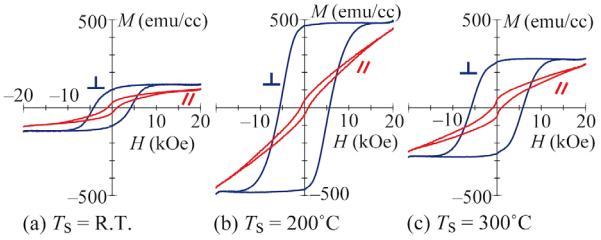

Fig. 15 M-H loops of MnGa (15 nm) films on Si substrate grown at various temperatures T_s.

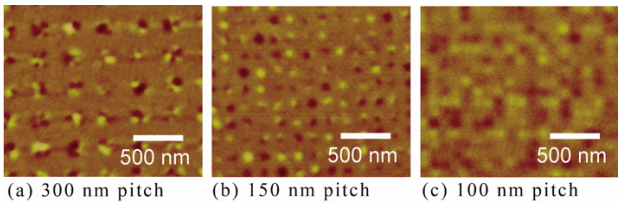

Fig. 16 MFM images of dot-patterned MnGa (15 nm) film fabricated by 30 keV Kr^+ ion dose of 1×10^{14} ions/cm^2.

homogeneity of the MnGa films on Si substrates is necessary for practical application.

In order to fabricate smaller dot patterns of MnGa film on Si substrate, the MnGa layer thickness was reduced to 5nm, whereas the M_s substantially decreased. Therefore, the insertion of CoGa buffer layer was employed since it was confirmed to be effective for reduction of the thickness of MnAl films. Figure 17 shows the XRD profiles of Cr(2 nm)/MnGa(5 nm)/CoGa(30 nm)/Cr(20 nm)/MgO(20 nm)/CrB(5 nm)/NiTa(25 nm)/SiO_2/Si substrate films, where Cr/MgO/CrB/NiTa layers were annealed at 800˚C and then CoGa buffer layer was annealed at T_a^{CoGa} for 30 minutes after deposition at 400˚C[39]. After the preparation of the buffer layers, the MnGa layer was grown at 200˚C and annealed at 400˚C for 60 min. The 001 and 002 peaks from the

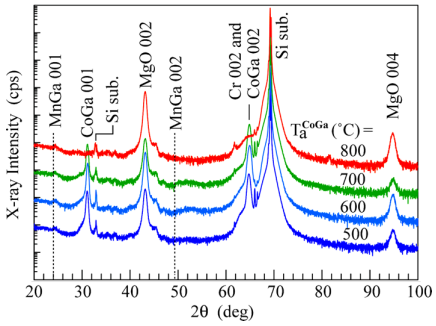

Fig. 17 X-ray profiles of MnGa (5 nm) films on Si substrate for samples with various annealing temperatures T_a^{CoGa} for CoGa buffer layer.

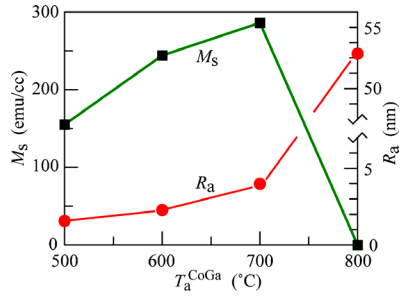

Fig. 18 Dependence of M_s and average surface roughness R_a of MnGa (5 nm) films on Si substrate on annealing temperature T_a^{CoGa} of CoGa buffer layer.

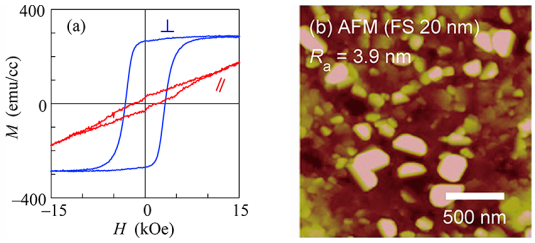

Fig. 19 *M-H* loops (a) and AFM image (b) of MnGa (5 nm) film with T_a^{CoGa} = 700˚C.

CoGa layer was clearly seen in the XRD profiles while the peaks from $L1_0$ phase of MnGa layer were very weak due to its reduced thickness. Figure 18 shows the T_a^{CoGa} dependence of M_s and average surface roughness R_a of the MnGa films on Si substrates. The M_s increases with increasing T_a^{CoGa} and takes a peak value at 700˚C while the roughness is degrading with T_a^{CoGa}. Figure 19 shows *M-H* loops and AFM image of the MnGa film of T_a^{CoGa}=700˚C. This film shows large M_s, large perpendicular anisotropy and good squareness, which are similar to the film on MgO substrate shown in Fig. 9 (b). However, improvement of the large surface roughness is necessary for the application to recording media.

6. Summary

In this paper, the crystal structure, magnetic and magneto-optical properties of CoPt, $MnPt_3$, $CrPt_3$, MnAl and MnGa films with ordered phase and the dot patterning by ion irradiation are reviewed. The CoPt films grown on a heated MgO(111) substrate have $L1_1$ phase, which does not appear in Co-Pt phase diagram, and exhibit large perpendicular anisotropy. The $CrPt_3$ films with $L1_2$ phase show large perpendicular anisotropy due to magneto-elastic effect. By utilizing the change from $L1_2$ to disordered phase caused by the low dose Kr^+ ion irradiation, dot patterns of $CrPt_3$ film with flat surface were successfully prepared. It is found that the CoGa buffer layer is effective to grow thinner $L1_0$ MnAl and MnGa films on MgO(001) substrate with keeping (001) orientation. In the case of fabrication of MnGa on SiO_2/Si substrates, the buffer layer of CoGa/Cr/MgO/Cr/NiTa is necessary to grow $L1_0$ MnGa with (001) orientation. The ordered alloy films described in this review are considered to be useful materials for magnetic recording and spintronics technology.

Acknowledgment The authors would like to thanks to the students who performed a lot of experiments in our laboratory and to M. Kumazawa for his dedicated assistance in experiments.

References

1) P.F. Carcia, A. D. Meinhaldt and A. Suna: *Appl.Phys.Lett.* **47**, 178 (1985) .
2) R.F. Carcia : *J. Appl. Phys.*, **63**, 5066 (1988) .

3) K.Nakamura, S.Tsunashima S.Iwata S.Uchiyama : *IEEE Trans. Magn.*, **25**, 3758 (1989).
4) D. Weller, H. Brandle, G. Gorman, C. -J. Lin, H. Notarys : *Appl. Phys. Lett.*, **61**, 2726 (1992).
5) M.R. Visokay, R. Sinclair : *Appl.Phys.Lett.*, **66**, 1692 (1995).
6) B. M. Lairson, M. R. Visokay, E. E. Marinero, R. Sinclair, and B. M. Clemens : *J. Appl. Phys.*,**74**, 1922(1993).
7) S. Iwata, S. Yamashita, and S. Tsunashima : *IEEE Trans. Magn.*, **33**, 3670 (1997)
8) T. Kato, S. Iwata, S. Yamashita, H. Takewaka, T. Kogiso, and S. Tsunashima : *J. Magn. Soc. Jpn.*, **23**, 47 (1999).
9) S. Iwata, S. Yamashita, and S. Tsunashima: *J. Magn. Magn. Mat.*, **198-199**, 381 (1999).
10) J. Cho, M. Park, H-S. Kim, T. Kato, S. Iwata, and S. Tsunashima : *J. Appl. Phys.*, **86**, 3149 (1999).
11) T. Kato, H. Ito, K. Sugihara, S. Tsunashima, and S. Iwata: *J. Magn. Magn. Mat.*, **272-276**, 778 (2004).
12) T. Kato, Y. Yamauchi, S. Iwata, S. Tsunashima, K. Matsumoto, T. Morikawa, K. Ozaki : *J. Appl. Phys.*, **105**, 07C117-1 (2009).
13) T. Kato, S. Iwata, Y. Yamauchi, S. Tsunashima : *J. Appl. Phys.*, **106**, 053908-1 (2009).
14) D. Oshima, E. Suharyadi, T. Kato, S. Iwata : *J. Magn. Magn. Mat.*, **324**, 1617 (2012).
15) H. Kurt, K. Rode, M. Venkatesan, P. Stamenov, and J. M. D. Coey : *Phys. Rev. B*, **83**, 020405 (2011).
16) B. Balke, G. H. Fecher, J. Winterlik, and C. Felser : *Appl. Phys. Lett.*, **90**, 152504 (2007) .
17) S. Mizukami, F. Wu, A. Sakuma, J. Walowski, D. Watanabe, T. Kubota, X. Zhang, H. Naganuma, M. Oogane, Y. Ando, and T. Miyazaki : *Phy. Rev. Lett.*, **16**, 117201 (2011).
18) S. H. Nie, L. J. Zhu, J. Lu, D. Pan, H. L. Wang, X. Z. Yu, J. X. Xiao, and J. H. Zhao : *Appl. Phys. Lett.*, **102**, 152405 (2013).
19) D. Oshima, T. Kato, S. Iwata, S. Tsunashima : *IEEE Trans. Magn.*, **49**, 3608 (2013).
20) T. Kato, D. Oshima, S. Iwata : *Crystals* **9**, 27-1 (2019)
21) R.A. McCurrie, P.Gaunt : *International Conference on Magnetism*, Nottingham, England, p. 780 (1964).
22) H. Sato, T. Shimatsu, Y. Okazaki, H. Muraoka, H. aoi, S. Okamoto, and O. Kitakami : *J. Appl. Phys.*,**103**, 07E114 (2008).
23) P. G. van Engen, K. H. J. Buschow, R. Jongebreur and M. Erman : *Appl. Phys. Lett.*, **42**, 202 (1983).
24) A.Cebollada, D. Weller, J. Sticht, G. R. Harp, R. F. C. Farrow, R. F. Marks, R. Savoy and J. C. Scott : *Phys. Rev. B*, **50**, 3419 (1994).
25) G. Q. Di, S. Iwata, S. Tsunashima and S. Uchiyama : *J. Magn. Magn. Mat.*, **104**, 1023 (1992).
26) T. Kato, H. Kikuzawa, S. Iwata, S. Tsunashima, and S. Uchiyama : *J. Magn. Magn. Mat.*, **140-144**, 713 (1995).
27) S. Iwata, T. Kato, M. Kokuryu, and S. Tsunashima : *J. Magn. Soc. Jpn.*, **20-S1**, 427 (1996).
28) T. Kato, S. Iwata, M. Kokuryu, and S. Tsunashima : *J. Magn. Soc. Jpn.*, **22**, 85(1998).
29) T. Kato, K. Sugihara, A. Kobayashi, S. Iwata, and S. Tsunashima : *IEEE Trans. Magn.*, **37**, 2414 (2001)
30) O. Hellwig, D. Weller, A. J. Kellock, J. E. E. Baglin, and E. E. Fullerton : *Appl. Phys. Lett.* **79**, 1151 (2001).
31) S. Mizukami, T. Kubota, F. Wu, X. Zhang, and T. Miyazaki : *Phys. Rev. B*, **85**, 014416 (2012).
32) M. Hosoda, M. Oogane, M. Kubota, T. Kubota, H. Saruyama, S. Iihama, H. Naganuma, and Y. Ando : *J. Appl. Phys.*, **111**, 07A324 (2012).
33) D. Oshima, M. Tanimoto, T. Kato, Y. Fujiwara, T. Nakamura, Y. Kotani, S. Tsunashima, S. Iwata : *IEEE Trans. Magn.*, **50**, 3203407-1 (2014).
34) D. Oshima, T. Kato, S. Iwata : *AIP Adv.*, **10**, 025012-1 (2020).
35) K. Z. Suzuki, R. Ranjbar, A. Sugihara, T. Miyazaki, and S. Mizukami : *Jpn. J. Appl. Phys.* **55**, 010305 (2016).
36) K. Z. Suzuki, R. Ranjbar, J. Okabayashi, Y. Miura, A. Sugihara, H. Tsuchiura, and S. Mizukami : *Sci. Rep.*, **6**, 30249 (2016).
37) J. Wang, Y. K. Takahashi, K. Yakushiji, H. Sepehri-Amin, H. Kubota, and K. Hono : in *Proc. 61st Annu. Conf. Magn. Magn. Mater.*, HH-07 (2016).
38) T. Ishikawa, Y. Miwa, D. Oshima, T. Kato, and S. Iwata : *IEEE Trans. Magn.*, **55**, 3200104 (2019).
39) Y. Miwa, D. Oshima, T. Kato, S. Iwata : *J. Magn. Soc. Jpn.*, **44**, 117 (2020).

Received May 01, 2021; Accepted July 19, 2021

J. Magn. Soc. Jpn., **45**, 125-130 (2021)

<Paper>

Reluctance Network Model of Interior Permanent Magnet Motor with Polar Anisotropic Magnet

Y. Hane, Y. Uchiyama, and K. Nakamura

Graduate School of Engineering, Tohoku Univ., *6-6-11 Aoba Aramaki, Aoba-ku, Sendai 980-8579, Japan*

To establish a practical method for analyzing interior permanent magnet (IPM) motors that have complicated flux distribution, this paper presents a method for deriving an analytical model for the IPM motor with polar anisotropic magnets, based on a reluctance network analysis (RNA). The proposed model can calculate the basic characteristics of the IPM motor with high accuracy and high speed by comparing the calculation results with the FEM and experiment.

Key words: interior permanent magnet (IPM) motor, reluctance network analysis (RNA), polar anisotropic magnet

1. Introduction

In recent years, electrification has been promoted in various fields such as industry, transportation, and people's livelihood so that the demand for motors has been expanding. Among various types of motors, utilization of a permanent magnet (PM) motor has been extremely increasing due to the rapid development of power electronics technology and the significant performance improvement of permanent magnets. PM motors can be divided into a surface permanent magnet (SPM) motor and an interior permanent magnet (IPM) motor. Among them, an IPM motor generally has high output and efficiency characteristics because it can utilize the reluctance torque generated from the magnetic saliency, in addition to the magnet torque. To further improve the performances of IPM motors, it is necessary to design not only the motor structure but also the control system. However, in the design and analysis based on a finite element method (FEM), it is not necessarily practical to perform the coupled analysis of the electromagnetic and control systems, which generally requires a long calculation time and a large computer memory.

To solve the above problem, we have proposed a reluctance network analysis (RNA), which expresses an analytical object by one reluctance network. All the reluctances can be determined by the *B-H* curve of the material and dimensions [1]. The RNA has some advantages such as a simple model, fast calculation, and easy coupling with external electric circuits and motion equation. The RNA has been applied to the calculation of characteristics of various electric machines including motors [2)-7)]. In the previous papers on the RNA, the SPM motors were often used as objects of discussion. In most of these considerations, the RNA models are relatively coarsely divided, and their rotational motions are expressed by only switching the positive and negative of the MMFs generated from the permanent magnets, that is, the circuit topology does not change.

On the other hand, only the IPM motors with relatively simple structures such as an inset type were examined for the RNA. This fact seems to be due to the model complexity. To express the complicated flux distribution with high accuracy, it is necessary to finely divide the RNA model into a large number of elements in the same manner as the FEM in general. However, in this way, the calculation time and cost increase as the model scale becomes larger, and the model construction becomes too complicated since the MMFs in each divided element should be intricately changed depending on the rotor position angle. In contrast, in a few papers on the RNA, the reluctance connections between the stator and rotor are switched with rotations [8)]. However, this technique leads to low calculation speed and constraints on the fineness of division due to deterioration of solution convergence. Thus, the original requirements of the RNA cannot be satisfied so far.

Therefore, this paper presents a method for deriving the RNA model which can express the flux distribution with necessary and sufficient calculation accuracy without fine model division. In this way, it is possible to analyze with practical calculation time and cost even when the RNA is applied to IPM motors with complicated structures. Among IPM motors with various structures which have been proposed so far, this paper focuses on the one which has neodymium-bonded magnets magnetized with polar anisotropy. In this paper, the basic characteristics of the IPM motor are calculated by using the proposed RNA model, and its validity is proved by comparing the calculation results with the FEM and experiment.

2. Derivation of RNA Model for IPM Motor with Polar Anisotropic Magnets

2.1 Basic configuration of IPM motor

Fig. 1(a), (b), and (c) show the IPM motor used in the consideration and its rotor structure. The magnet material is bonded Nd-Fe-B magnet, the recoil permeability is 1.275, and the coercive force is 461 kA/m. Besides, as shown in Fig. 1(c), the rotor magnets are

Corresponding author: Y. Hane (e-mail: yoshiki.hane.e2@tohoku.ac.jp).

magnetized in the arcuate direction, not in the general radial and parallel ones, so that the flux concentrates at the center of the magnetic pole. As a result, the gap flux distribution becomes almost sinusoidal, and the amplitude of the fundamental wave component, which contributes to the torque, increases [9), 10)].

2.2 Derivation method of RNA model

Fig. 2 shows the simplified view of the proposed RNA model of one pole of the IPM motor. This model is halved in the *z*-axis direction in consideration of the magnetic field symmetry. As shown in this figure, each divided element is expressed by a reluctance element, whose parameters can be determined by the *B-H* curve of the material and dimensions of the divided elements. In the following, the derivation method of the proposed model is described in detail for each part of the IPM motor.

First, the derivation method of the magnetic circuit of the stator is explained [1)]. Each reluctance in the stator core has to be determined in consideration of the nonlinear magnetic properties. Besides, it is preferable to express the *B-H* curve by using an approximate equation rather than a look-up table from the view point

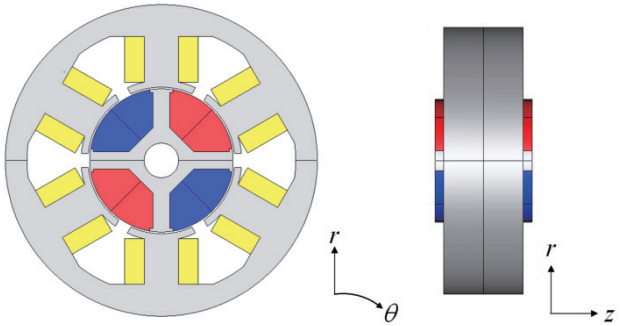

(a) External view.

(b) Specifications.

Diameter	54 mm
Stack length of stator	16 mm
Stack length of rotor	19.5 mm
Gap length	0.3 mm
Number of turns/pole	24 turns/pole
Winding diameter	1.2 mm
Magnet pole pairs	2
Material of magnet	Bonded Nd-Fe-B
Material of iron core	35A300

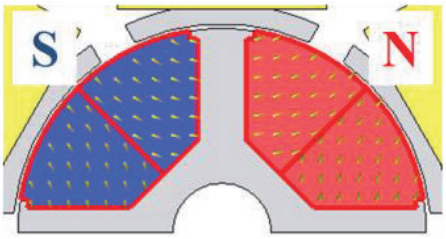

(c) Rotor structure.

Fig. 1 IPM motor used in the consideration.

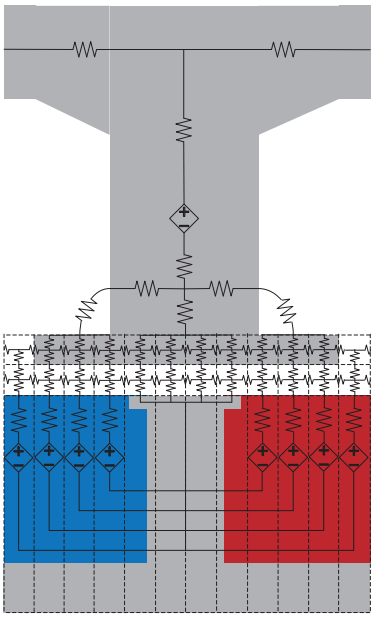

Fig. 2 Simplified view of the RNA model of one pole of the IPM motor.

of solution convergence. Here, the magnetic nonlinearity is given by

$$H = \alpha_1 B + \alpha_m B^m \tag{1}$$

where the coefficients are α_1 = 51 and α_m = 2.5, respectively. The order m = 15 is determined by the strength of the nonlinearity of the *B-H* curve. Fig. 3 shows the measured *B-H* curve of the core material and its approximated curve. From the equation (1), the relationship between the MMF $f_m = Hl$ and the magnetic flux $\phi = BS$ in each reluctance can be expressed by the following equation:

$$f_m = \left(\frac{\alpha_1 l}{S} + \frac{\alpha_m l}{S^m} \phi^{m-1} \right) \phi \tag{2}$$

where the average cross-sectional area and magnetic path length of each element are S and l, respectively. Therefore, the nonlinear reluctance R_m is given by the following equation:

$$R_m = \frac{\alpha_1 l}{S} + \frac{\alpha_m l}{S^m} \phi^{m-1} \tag{3}$$

Next, the air region surrounding the stator core is also included in the analytical model so that the leakage flux between the center and tip of the stator pole can be taken into consideration. The reluctance in the air region is simply given by the following equation:

$$R_a = \frac{l}{\mu_0 S} \tag{4}$$

where the vacuum permeability is μ_0. Besides, the MMF generated by the winding current is concentrated in which the winding is applied.

On the other hand, the stator pole tips, air gaps, and rotor magnets, where the flux distribution is more complicated, are divided into 360 in increments of 1 degree in the circumferential direction. Here, the reluctances in the rotor core are neglected since they are

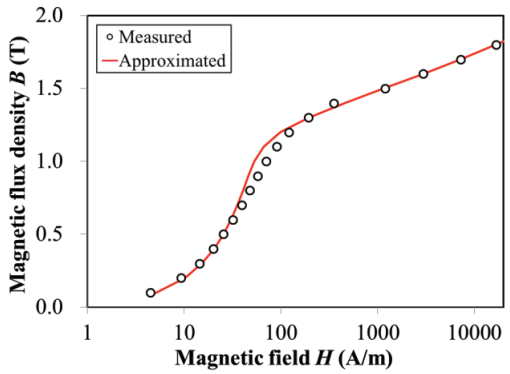

Fig. 3 *B-H* curve of core material and its approximated curve.

extremely smaller than those in the magnets, whereas those in the stator core must be considered due to the relatively high flux density in the poles, which are the main flux paths, and the local saturation at the pole tips. The reluctances in the stator pole tips and air gaps are represented by using the equations (3) and (4), respectively. Further, the reluctances R_p and MMF F_c in the magnets are given by the following equations:

$$R_p(\theta) = \frac{|l_p(\theta)|}{\mu_0 \mu_r S} \tag{5}$$

$$F_c(\theta) = H_c l_p(\theta) \tag{6}$$

where the recoil permeability is μ_r and the coercive force is H_c, respectively. The effective length $l_p(\theta)$ in the arc-shaped magnetized direction, changes depending on the rotor position angle θ as shown in Fig. 4(a) and (b), and is given by the Fourier series as follows:

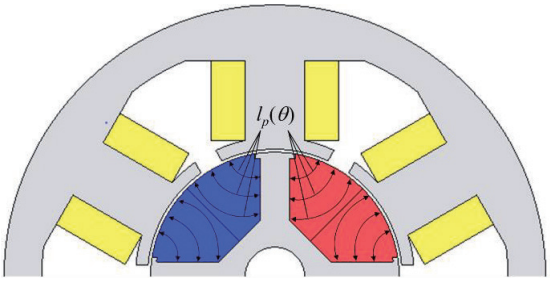

(a) Where $l_p(\theta)$ points.

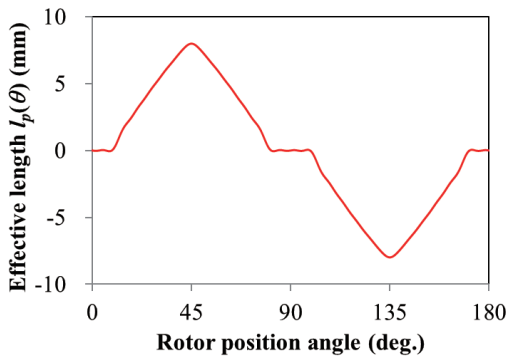

(b) Relationship between the rotor position angle θ and the effective length $l_p(\theta)$.

Fig. 4 Effective length $l_p(\theta)$ of the permanent magnet corresponding to the rotor position angle θ.

$$l_p(\theta) = \sum_{j=1}^{N} a_j \cos 2(2j-1)\theta \tag{7}$$

where the coefficient is N = 15. In this way, the complicated flux distribution of the rotor with polar anisotropic magnets can be expressed with a simple model, compared to a finely divided FEM model.

Moreover, some flux flows into the laminated surface of the stator core from the protruding rotor magnets and leaks into the air region since this IPM motor has an overhang structure. To strictly consider it, a three-dimensional magnetic circuit is generally required. However, it is expected that the calculation time increases as the model becomes larger. Thus, to simply represent the overhang structure, each circumferential element in the protruding parts of the rotor magnets is connected to the laminated surface at the opposing stator pole tips and the leakage reluctances from all other circumferential elements, as shown in Fig. 5.

3. Simulation Results by Using Proposed Method

In this chapter, the basic characteristics of the IPM motor are calculated by using the proposed RNA model. The RNA is performed by using Ansys Twin Builder 2021 R1, which is the general-purpose circuit simulator. In the analysis, the three-phase sinusoidal current is input when the current phase angle is 18 deg., and the rotational speed of the IPM motor is constant at 12600 rpm. The RNA calculation results are validated by comparing with the experimental and FEM calculation ones. In the experiment, characteristics of the IPM motor are obtained by measuring input current and

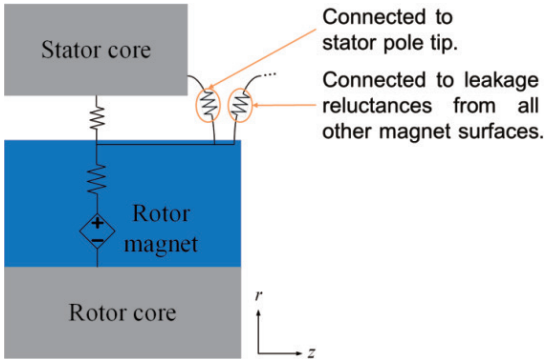

Fig. 5 Magnetic circuit in the overhang part.

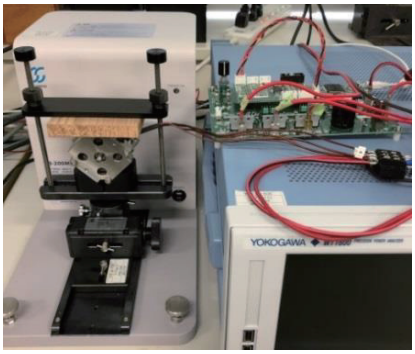

Fig. 6 Experimental setup.

power when the motor is arbitrarily loaded while driven by a PWM converter at a constant rotational speed of 12600 rpm, using the system as shown in Fig. 6. The FEM is conducted by using JMAG-Designer Ver.20.0, which is the general-purpose electromagnetic field analysis software.

Fig. 7(a) and (b) show the comparisons of the calculated flux density waveforms flowing through the center of the stator pole, between the RNA and FEM. From these figures, it is understood that both results are in good agreement.

Fig. 8 shows the measured and calculated winding current density versus torque characteristics. From this figure, it is clear that the calculation results of the RNA and FEM are in good agreement. On the contrary, the measured and calculated results are almost in good agreement though there is a little error, whose cause is that the iron and mechanical losses are neglected in the analysis.

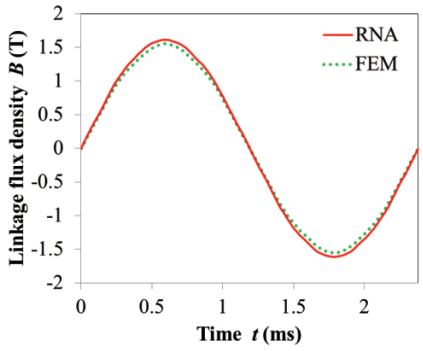

(a) Winding current density is 0 A/mm^2.

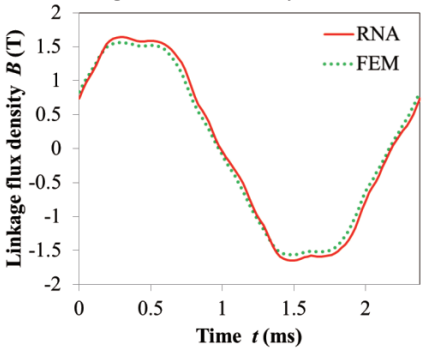

(b) Winding current density is 7 A/mm^2.

Fig. 7 Flux density waveforms flowing through the stator pole center.

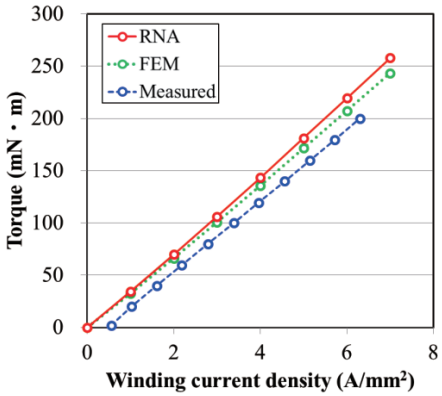

Fig. 8 Winding current density versus torque characteristics.

4. Calculation Considering Iron Loss

4.1 RNA model of IPM motor considering iron loss

In this section, the derivation method of the improved RNA model which can consider the iron loss in a simple way [11] is described, to further increase the calculation accuracy of the above-proposed RNA model.

Fig. 9 shows the RNA model of the IPM motor considering the iron loss. As shown in this figure, each part in the stator core is expressed by connecting an inductance element representing the iron loss in series with the reluctance given by the equation (3). Here, the relationship between the MMF f_m and the magnetic flux ϕ in each divided element can be expressed by the following equation:

$$f_m = \left(\frac{\alpha_1 l}{S} + \frac{\alpha_m l}{S^m} \phi^{m-1} \right) \phi + \frac{\beta_1 l}{S} \frac{\mathrm{d}\phi}{\mathrm{d}t} = R_m \phi + L_m \frac{\mathrm{d}\phi}{\mathrm{d}t} \tag{8}$$

where the coefficient is β_1 = 0.0438, which can be approximately determined by fitting the core loss curves of the materials by the least squares method based on the following equation:

$$W_i = \frac{2\pi^2 \beta_1}{q} f^2 B_m{}^2 \tag{9}$$

where the iron loss per unit weight is W_i, the mass density is q, the frequency is f, and the maximum flux density is B_m, respectively. In this way, it is possible to calculate the iron loss without post-processing using the Steinmetz' equation [12] in the RNA.

4.2 Iron loss and efficiency calculation results

In this section, the analysis is performed by using the improved RNA model under the same conditions as in Chapter 3. The validity of the RNA calculation results is verified by comparing with the experimental and FEM calculation ones.

Fig. 10 shows the measured and calculated winding current density versus torque characteristics. This figure reveals that the calculated values of the RNA are somewhat closer to the measured ones than those shown in Fig. 8 by considering the iron loss. On the other hand, there are still some errors since the mechanical loss is not taken into account in the analysis.

Fig. 11 shows the measured and calculated iron loss characteristics. In the RNA, the iron loss is calculated by taking the sum of the products of the MMF and the time derivative of the flux in each divided element. On the other hand, in the FEM, FFT is performed on the flux density waveforms in each element obtained from the electromagnetic field analysis, and the iron loss is calculated by applying the Steinmetz' equation to the waveforms of each order [12]. From the figure, it is clear that the calculated values of the RNA and FEM are in

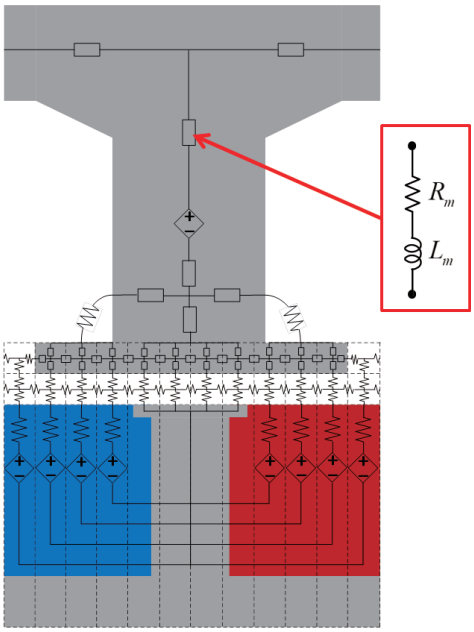

Fig. 9 Simplified view of the RNA model of one pole of the IPM motor which can consider the iron loss.

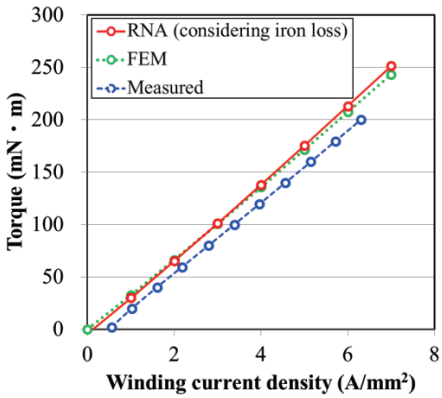

Fig. 10 Winding current density versus torque characteristics considering the iron loss in the RNA.

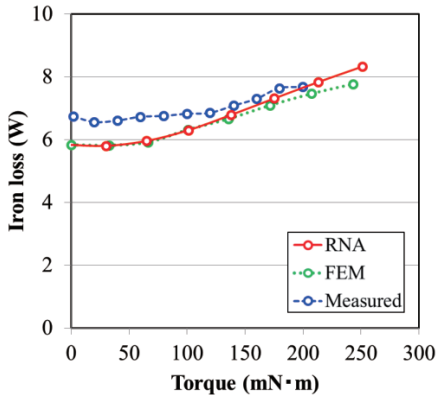

Fig. 11 Iron loss characteristics.

good agreement. On the contrary, when comparing the RNA calculation results and experimental ones, it can be seen that both are almost in good agreement at high load, while the errors are larger at low load. The cause of the errors is that the additional loss generated by the carrier harmonics in the measured current waveforms, as shown in Fig. 12(a) and (b), is not taken into consideration in the analysis. It is known that the iron loss cannot be accurately calculated when this RNA model is applied to a complicatedly distorted excitation waveform [13]. Therefore, a further increase in the calculation accuracy is indispensable by improving the current RNA model.

Fig. 13 shows the measured and calculated efficiency characteristics. In the RNA and FEM, to calculate the efficiency including the mechanical loss, the measured values are substituted. From this figure, it is understood that the calculated and measured results are in good agreement.

Table 1 shows the comparison of the calculation time per one cycle of electric angle between the RNA and

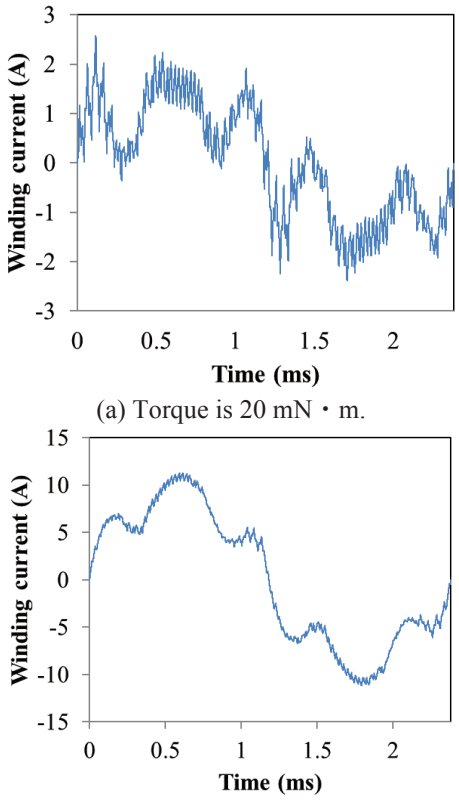

(a) Torque is 20 mN・m.

(b) Torque is 200 mN・m.

Fig. 12 Measured current waveforms.

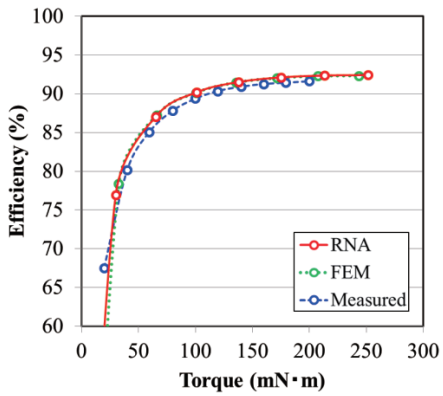

Fig. 13 Efficiency characteristics.

Table 1 Comparison of calculation time per one cycle between RNA and FEM.

Winding current density (A/mm^2)	RNA calculation time (s)	FEM calculation time (s)
0	15.0	3237.5
1	15.0	3236.5
2	15.0	3285.0
3	15.0	3342.5
4	15.0	3301.5
5	15.0	3222.5
6	15.5	3293.5
7	15.5	3381.0

FEM. Here, the RNA is non-parallel computation, while the FEM is conducted by using two processor cores. The numbers of calculation steps per one cycle in the RNA and FEM are 240 and 180, respectively. As shown in the table, the RNA calculation time is less than 1% of that of the FEM in each case, which indicates that the proposed RNA model is excellent from the view point of not only the calculation accuracy but also the calculation speed.

5. Conclusion

This paper presented a method for deriving the RNA model of the IPM motor with the complicated structure, by using the one which has polar anisotropic magnets as a representative. As a result of the consideration, it is clarified that the proposed RNA model can calculate several characteristics of the IPM motor with high accuracy. Besides, in this way, it is possible to construct the relatively simple model without problems such as an increase in model scale and deterioration of solution convergence. In the future, we plan to study the following two things:

(1) To more accurately calculate the iron loss including the minor loop when the IPM motor is driven by a PWM converter by incorporating the play model [14] and Cauer circuit [15], as suggested in the previous paper [16].

(2) To derive a simple RNA model for IPM motors with other various structures, such as when magnets are arranged in a V-shape.

Acknowledgements This work was supported by Grant-in-Aid for JSPS Fellows (JP19J20572).

References

1) K. Nakamura and O. Ichinokura, *IEEJ Trans. FM*, **128**, 506 (2008).
2) K. Nakamura, K. Kimura, and O. Ichinokura, *J. Magn. Magn. Mat.*, **290-291**, 1309 (2005).
3) M. Fukuoka, K. Nakamura, and O. Ichinokura, *IEEE Trans. Magn.*, **47**, 2414 (2011).
4) K. Nakamura, K. Honma, T. Ohinata, K. Arimatsu, T. Shirasaki, and O. Ichinokura, *J. Magn. Soc. Jpn.*, **38**, 174 (2014).
5) Y. Hane, H. Tanaka, and K. Nakamura, *J. Magn. Soc. Jpn.*, **2**, 25 (2018) [in Japanese].
6) Y. Hane and K. Nakamura, *Proc. IEEE Int. Magn. Conf. (INTERMAG 2018)*, 1800038 (2018).
7) Y. Hane, K. Nakamura, T. Ohinata, and K. Arimatsu, *IEEE Trans. Magn.*, **55**, 8401306 (2019).
8) Y. Yoshida, K. Nakamura, and O. Ichinokura, *IEEE Trans. Magn.*, **48**, 3108 (2012).
9) S. Kitamura, Y. Ishihara, T. Todaka, and Y. Inoue, *IEEJ Trans. IA*, **117**, 1001 (1997) [in Japanese].
10) M. Fukuoka, K. Nakamura, and O. Ichinokura, *J. Magn. Soc. Jpn.*, **36**, 123 (2012) [in Japanese]
11) K. Tajima, O. Ichinokura, A. Kaga, and Y. Anazawa, *J. Magn. Soc. Jpn.*, **19**, 553 (1995) [in Japanese].
12) C. P. Steinmetz, *Proc. IEEE*, **72**, 197 (1984).
13) H. Tanaka, *Ph. D. thesis in Tohoku University* (2017) [in Japanese].
14) S. Bobbio, G. Miano, C. Serpico, and C. Visone, *IEEE Trans. Magn.*, **33**, 4417 (1997).
15) Y. Shindo and O. Noro, *IEEJ Trans. FM*, **134**, 173 (2014).
16) Y. Hane and K. Nakamura, *IEEE Trans. Magn.*, **56**, 6703306 (2020).

Received Apr. 16, 2021; Accepted Jul. 18, 2021

J. Magn. Soc. Jpn., **45**, 131-135 (2021)

<Paper>

Magnetocardiography Current Source Estimation using Multiple Spatial Filters

K. Kobayashi*, M. Iwai*, Y. Ono*, W. Sun**, M. Sugimachi***, K. Kusano***, and T. Shishido***

*Faculty of Science and Engineering, Iwate Univ., *4-3-5 Ueda, Morioka, Iwate 020-8551, Japan*

**Faculty of Engineering, Kindai Univ., *1-Takaya Umenobe, Higashihiroshima, Hiroshima 739-2116, Japan*

***National Cerebral and Cardiovascular Center Research Institute, *6-1 Kishibe-Shimmachi, Suita, Osaka 564-8565, Japan*

In this study, cardiac current source localization was simulated using the spatial filter method. We estimated current sources using data from two measurement surfaces, i.e., the front and back of the subject, to reduce the large spatial extension in the depth direction. Three methods for creating spatial filters were developed using the exact low-resolution brain electromagnetic tomography method based on different creation procedures. The first method is a general method that has been conventionally used to create a spatial filter (64ch spatial filter) using a 64ch sensor on the front side. The second method is to create a spatial filter (128ch spatial filter) using two 64ch sensors on the front and back sides as a 128ch sensor. The third method is to create two spatial filters separately and use them as one spatial filter (2 × 64ch spatial filter). In this case, different Tikhonov regularization parameters can be determined on the front and back sides, and optimum noise immunity can be given to each. The accuracy of the estimated current sources using the three types of spatial filters was examined using simulation and MCG data. The results show that the 2 × 64 spatial filter has the highest estimation accuracy and suppresses the large spatial extension of the estimated current sources.

Key words: magnetocardiography, current source estimation, spatial filter, eLORETA

1. Introduction

Magnetocardiography (MCG) is a noninvasive technique used for detecting the magnetic field generated by electrical activities in the heart. Recently, its efficacy in the early detection of heart diseases has been evaluated [1], and its multichannel measurements, which are unaffected by the shape of the lungs and torso, have been used in clinical applications [2]. MCG aims to obtain functional mapping, starting from the visualization of signal sources. Because the MCG inverse problem is ill-posed and does not have a unique solution, the estimation of MCG signal sources is the biggest challenge for its application [3]. In the past decades, the equivalent current dipole model has been used for MCG source localization; however, single or several dipoles cannot efficiently explain measured data. Recently, the spatial filter method has been used to visualize cardiac activities. This method was developed for MCG source localization and can be used to obtain a reliable three-dimensional outline of the heart [4, 5]. MCG current sources are modeled by many current dipoles of a fixed location, orientation, and variable strength. As the unknowns are more than the knowns, the inverse problem is ill-posed. Generally, the ill-posed problem can be approached by minimum-norm least squares estimation (MNLE). However, it always favors sources that are close to the magnetic field sensors and leads to the reconstruction of blurred source imaging for deep sources. A weighting matrix was used to remove the depth bias for the weighted MNLE method [6]. Lead field normalization was performed to compensate for the varying sensitivities of the sensors to the current sources at different depths [7]. These methods could be suppressed the spread of deep sources. However, when the data in only one measurement plane is used, a sufficient suppressing effect is not obtained. Therefore, we proposed the method using two planes data [8]. First, the current source is estimated using one plane (MCG data). Next, the magnetic field distribution in the opposite plane is calculated using the estimated current source. This method is the current source estimation based on two planes data using the measurement MCG data and calculated magnetic field distribution in the opposite direction. However, in current source estimation using these measurement surfaces, the estimated current sources cannot be obtained at the correct position.

In this study, we attempted to estimate the current sources using data from the two measurement surfaces, i.e., the front (chest) and the back of the subject, to reduce the large spatial extension for deep sources. In reference 8, a standardized low-resolution brain electromagnetic tomography (sLORETA) [9] was used, but in this study, an exact low-resolution brain electromagnetic tomography (eLORETA) [10], which can further suppress the spread of the estimated current source, was used for MCG current source estimation. eLORETA is a non-adaptive spatial filter that can effectively localize the source with a proper Tikhonov regularization parameter [11]. In addition, we aim to reduce the large spatial extension for the depth direction of the estimated current sources and proposed the spatial filter creation method using two measurement planes. The accuracy of the estimated current sources was examined using simulation and MCG data.

2. Methods

2.1 eLORETA

eLORETA is a spatial filter method used to solve ill-posed problems. It can obtain a blurred source image

Corresponding author: K. Kobayashi
(e-mail: kobaya@iwate-u.ac.jp.)

using a linear inverse operator [10].

$$\boldsymbol{\Phi} = \boldsymbol{K}\boldsymbol{J} + \boldsymbol{n} \tag{1}$$

where $\boldsymbol{\Phi}$ is the detected signal, $\boldsymbol{K}$ is the lead-field matrix, $\boldsymbol{J}$ is the original current source within the heart, and $\boldsymbol{n}$ is the noise at each sensor. The eLORETA solution can be obtained as follows, and the estimated current sources $\hat{\boldsymbol{J}}$ can be written as

$$\hat{\boldsymbol{J}} = \boldsymbol{T}\boldsymbol{\Phi} \tag{2}$$

$$\boldsymbol{T} = \boldsymbol{W}^{-1}\boldsymbol{K}^{T}(\boldsymbol{K}\boldsymbol{W}^{-1}\boldsymbol{K}^{T} + \lambda\boldsymbol{I})^{-1} \tag{3}$$

$$\boldsymbol{W} = \{\boldsymbol{K}^{T}(\boldsymbol{K}\boldsymbol{W}^{-1}\boldsymbol{K}^{T} + \lambda\boldsymbol{I})^{-1}\boldsymbol{K}\}^{1/2} \tag{4}$$

where $\boldsymbol{T}$ is a spatial filter matrix, T denotes the matrix transpose, λ is the Tikhonov regularization parameter, $\boldsymbol{I}$ represents an identity matrix, and $\boldsymbol{W}$ denotes a symmetric weight matrix. The particular case of interest here is the structured block-diagonal weight matrix $\boldsymbol{W}$. $\boldsymbol{W}$ be obtained as follows,

1. Initialize the weight matrix $\boldsymbol{W}$ as an identity matrix $\boldsymbol{I}$.
2. Calculate a matrix $\boldsymbol{A}$,
$$\boldsymbol{A} = (\boldsymbol{K}\boldsymbol{W}^{-1}\boldsymbol{K}^{T} + \lambda\boldsymbol{I})^{-1} \tag{5}$$
3. Calculate the new weight $\boldsymbol{W}$,
$$\boldsymbol{W} = (\boldsymbol{K}^{T}\boldsymbol{A}\boldsymbol{K})^{1/2} \tag{6}$$
4. Using the new weight, go to step 2 until convergence (i.e. stop when the change in the weight matrix is sufficiently small).

In this paper, the convergence condition is that the inner product before and after the update of $\boldsymbol{W}$ is 1 (within 10^{-12}).

2.2 MCG measurements

The MCG data were measured using a 64-channel (8 × 8) SQUID magnetometer (MC-6400, Hitachi Ltd.) in a magnetically shielded room [12]. The MCG measurements were performed on two measurement surfaces, i.e., on the back and the front (chest) side, which is the conventional measurement surface. MCGs of the two subjects were measured. Approximately 30 trials were averaged to reduce the noise. This study was approved by the Ethics Committee of Iwate University (No. 202002).

2.3 Proposed methods to create spatial filters

We examined three types of spatial filter fabrication methods using the two measurement surfaces. The first method is a general method that has been conventionally used to create a spatial filter (64ch spatial filter) using a 64ch sensor on the front side. The second method is to create a spatial filter (128ch spatial filter) using two 64ch sensors on the front and back sides as a 128ch sensor.

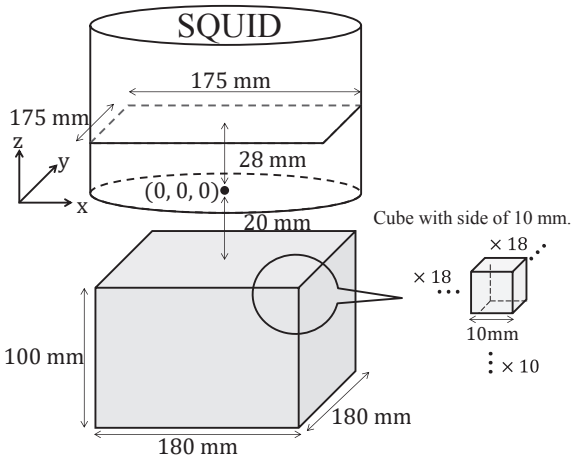

Fig. 1 Coordinate system and analysis conditions.

In this case, the Tikhonov regularization parameter λ has the same value on the front and back sides. The third method is to create two spatial filters separately and use them as one spatial filter (2 × 64ch spatial filter). In this case, different λ can be determined on the front and back sides, and the optimum noise immunity can be given to each. In this study, a spatial filter was created by setting λ to 1% of the maximum eigenvalue ($\boldsymbol{K}\boldsymbol{W}^{-1}\boldsymbol{K}^{T}$) in the second method, 1% of the maximum eigenvalue on the front side, and 5% on the back side in the third method. Here, 1% and 5% were determined by the signal-to-noise ratio of the MCG on the two measurement sides. At this time, a high estimation accuracy was obtained using these values. These values affect the estimation accuracy and need to be changed depending on the measurement conditions.

2.4 Coordinate system and analysis conditions

Fig. 1 shows the coordinate system and analysis conditions. The origin of the coordinates is the center of the bottom of the dewar of the SQUID magnetometer. The 64-channel sensor plane is at Z = 28 mm on the front side and Z = −218 mm on the back side. In this sensor arrangement, the front is located near the analysis space (48 mm) and the back is located far away (98 mm), assuming measurement by actual MCGs. The top voxel in the analysis space was Z = −20 mm. We estimated the MCG current sources within a 180 mm × 180 mm × 100 mm volume. A total of 3,240 voxels were divided, with the size of each voxel being 10 mm × 10 mm × 10 mm. For the forward problem, we calculated the lead-field matrix $\boldsymbol{K}$ using the Biot–Savart law. For each current source location, $\boldsymbol{K}$ includes two columns that represent the X and Y components.

3. Results and Discussions

3.1 Simulation results

To examine the effectiveness of the proposed methods, the current sources were estimated by a simulation. One signal source was set at coordinates (0, 0, −65) with a

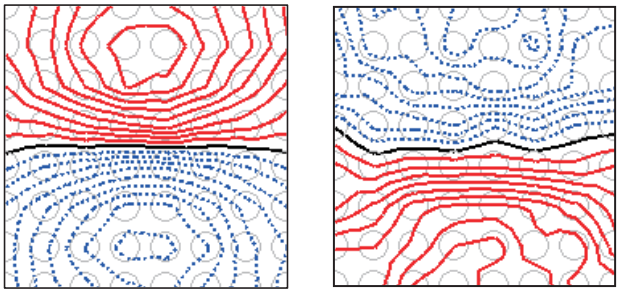

(a) Z = 28 mm (270pT/step) (b) Z = −218 (85pT/step)

Fig. 2 Calculated isofield contour maps.

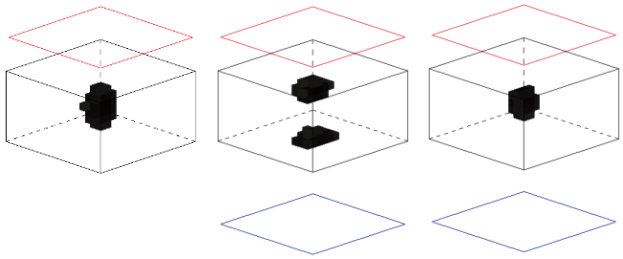

(a) 64ch (b) 128ch (c) 2×64

Fig. 3 Three types of estimation results: (a) 64ch spatial filter, (b) 128 spatial filter, and (c) 2 × 64 spatial filter.

signal strength of 1 μAm in the X direction. Uniform random noise of 5% of the maximum intensity was added to the calculated magnetic field. In the case of 5% uniform random noise, there was almost no effect of outliers. Fig. 2 shows the calculated isofield contour maps obtained by the simulation. The solid line indicates the positive direction of the z-axis, and the dotted line indicates the negative direction. Fig. 3 shows the estimation results of the three types of filters. Fig. 3(a) shows the estimation result of the 64ch spatial filter using one conventional measurement surface, Fig. 3(b) is the estimation result of the 128 spatial filter with two measurement surfaces as 128-channel sensors, and Fig. 3(c) is the estimation result of the 2 × 64 spatial filter in which spatial filters are individually created on the two measurement surfaces. In these figures, more than 90% of the maximum value of each estimated current source is shown as the estimated voxels. The top squares of Fig. 3(a), (b), and (c) and the bottom squares of Fig. 3(b) and (c) indicate the sensor surface, and the rectangular parallelepiped indicates the analysis space.

The estimated number of voxels was 47 for Fig. 3(a), 55 for Fig. 3(b), and 27 for Fig. 3(c). In addition, in Fig. 3(a), the estimated current sources were the large spatial extension in the deep direction; in Fig. 3(b), the estimated current sources were divided into a shallow part and a deep part and were not estimated correctly; and in Fig. 3(c), the estimated current sources were suppressed at the center and were estimated correctly. Therefore, the 2 × 64 spatial filter in Fig. 3(c) suppresses the spread of the estimated current sources in the depth direction.

3.2 MCG results

Fig. 4 shows the overlaid waveform of the 64-channel MCG of subject A on the front and back sides and the isofield contour maps of the R peak. Fig. 5 shows the estimated current sources of the R wave peak of subject A. Fig. 5 (a), (b), and (c) represent the estimated current sources of the three spatial filters, which are similar to the simulation study. The upper side is a view of the chest surface, and the lower side is the view of the heart from below. The square frame represents the analysis space. More than 90% of the maximum value of each estimated current sources (black areas) are shown as an estimated voxel on a cardiac model positioned from the current arrows map. The estimated current sources of 3D data are shown projected in 2D. The cardiac model was created from three-dimensional data of the heart, which was made by simulating the shape of a general heart by authors. In subject A, the estimated number of voxels was 64 for Fig. 5(a), 34 for Fig. 5(b), and 21 for Fig. 5(c).

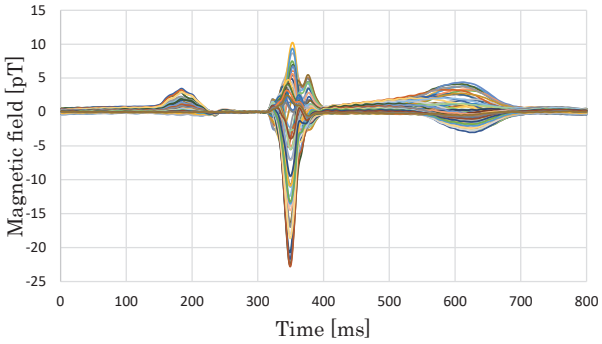

(a) Front side

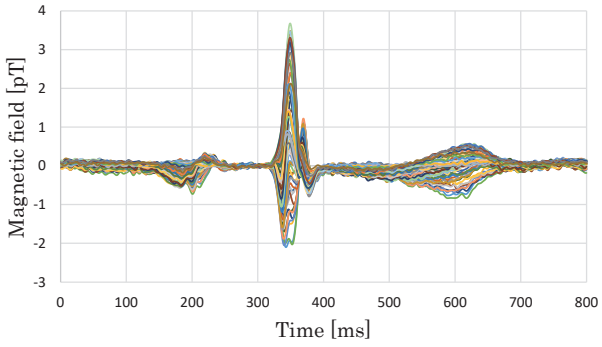

(b) Back side

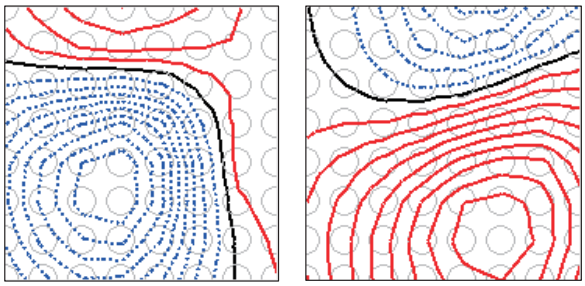

(c) Front side (2.3pT/step) (d) Back side (0.37pT/step)

Fig. 4 MCG waveforms and isofield contour maps of subject A.

(a) 64ch (b) 128ch (c) 2×64

Fig. 5 Estimated current sources of the R wave peak of subject A: (a) 64ch spatial filter, (b) 128 spatial filter, and (c) 2 × 64 spatial filter.

The estimated current sources of Fig. 5 (a) and (b) were divided into two, one was estimated near the atrium, and the estimation was not performed correctly. By contrast, in Fig. 5 (c), the estimated current sources existed in the lower part of the ventricle (called the apex of the heart), suggesting that it could be estimated the medically correct location.

Fig. 6 shows the overlaid waveform of the 64-channel MCG of subject B on the front and back sides and the isofield contour maps of the R peak. Fig. 7 shows the estimated current sources of the R-wave peak for subject B. In subject B, the estimated number of voxels was 62 for Fig. 7(a), 33 for Fig. 7(b), and 18 for Fig. 7(c). The estimated current sources of Fig. 7 (b) were near the atrium and could not be estimated correctly. The estimated current sources of Fig. 7 (a) and (c) were divided into two parts, which appeared in the atrium and ventricle. However, in Fig. 7 (c), the large spatial extension of the estimated current sources was suppressed compared to that in Fig. 7 (a), and a strong estimated current source was obtained in the lower part of the ventricle. Therefore, the 2 × 64 spatial filter of Fig. 7 (c) has the highest estimation accuracy and suppresses the large spatial extension of the estimated current sources.

These MCG results showed the following. In the 64ch spatial filter, since the measurement is one measurement plane, the estimated current source is spread. In the 128 spatial filter, the spread of the estimated current source can be suppressed. However, since the signal-to-noise ratio is different on the front and back sides, it cannot be estimated at the correct position. In the 2 × 64 spatial filter, the spread of the estimated current source can be suppressed. Furthermore, since the filter can be created according to the signal-to-noise ratio on the front and back side, the estimation accuracy is high.

4. Conclusions

We aim to reduce the large spatial extension of the estimated current sources by investigating the spatial filter creation method using two measurement planes.

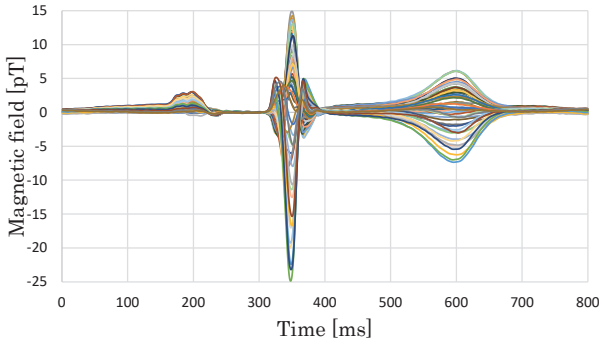

(a) Front side

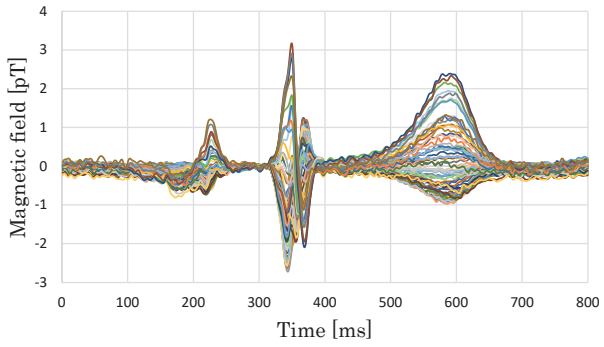

(b) Back side

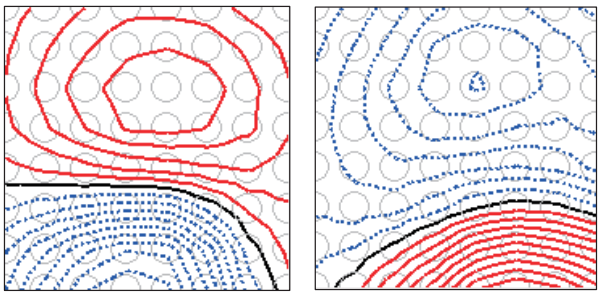

(c) Front side (2.5pT/step) (d) Back side (0.32pT/step)

Fig. 6 MCG waveforms and isofield contour maps of subject B.

(a) 64ch (b) 128ch (c) 2×64

Fig. 7 Estimated current sources of the R wave peak of subject B: (a) 64ch spatial filter, (b) 128 spatial filter, and (c) 2 × 64 spatial filter.

We propose three types of spatial filter methods of eLORETA using two-side measurements of the front and back of the body. The large spatial extension of the

estimated current sources can be further suppressed using the back and front sides. Among them, the signal source can be estimated at the correct position using a 2 × 64ch spatial filter that can determine the regularization parameter λ on the front and back sides, respectively. Visualization of the electrical heart activity is useful for diagnosis using MCG. In the future, the value of the Tikhonov regularization parameter is an important factor, we will consider how to determine the optimum value.

Acknowledgment This work was supported by Japan Society for the Promotion of Science KAKENHI (Grants-in-Aid for Scientific Research (C)) Grant Number JP19K12837 and the Soft-Path Science and Engineering Research Center,
Iwate University.

References

1) K. Tsukada, *et al.*,: *Int. J. Card. Imaging*, **16**, 5 (2000).
2) P. Takala *et al.*,: *Phys. Med. Biol.*, **46**, 975 (2001).
3) J. S. Kwong *et al.*,: *Int. J. Cardiol.*, **167**, 1835 (2013).
4) K. Nakai *et al.*,: *Int. J. Cardiovasc. Imaging*, **21**, 555 (2005).
5) Gauravi S. and Murugesh K.: *Int. J. Emerg. Technol. Innov. Res.*, **2**, 1156 (2015).
6) T. A. Crowley *et al.*,: in *Proc. Biomag96*, 197 (1996).
7) E. Palmero-Soler *et al.*,: *Phys. Med. Biol.*, **52**, 1783 (2007).
8) W. Sun and K. Kobayashi: *IEEE Trans. Magn.*, **53**, 1 (2017).
9) R. D. Pascual-Marqui: *Methods Find Exp. Clin. Pharmacol.*, **24**, 5 (2002).
10) R. D. Pascual-Marqui: *Mathmatical Phys.*, **0710**, 3341, ArXiv, (2007).
11) Y. Xu *et al.*: *Flow Meas. Instrum.*, **50**, 1 (2016).
12) H. Kanzaki *et al.*,: *Basic Res. Cardiol.*, **98**, 124 (2003).

Received May 03, 2021; Revised May 28, 2021; Accepted Jul. 06, 2021

Journal of the Magnetics Society of Japan

Vol. 45 No. 5 (通巻第317号) 2021年9月1日発行

Vol. 45 No. 5 Published Sep. 1, 2021
by the Magnetics Society of Japan
Tokyo YWCA building Rm207, 1–8–11 Kanda surugadai, Chiyoda-ku, Tokyo 101–0062
Tel. +81–3–5281–0106 Fax. +81–3–5281–0107

Printed by JP Corporation Co., Ltd.
Sports Plaza building 401, 2–4–3, Shinkamata Ota-ku, Tokyo 144–0054
Advertising agency: Kagaku Gijutsu-sha

発行：(公社)日本磁気学会 101–0062 東京都千代田区神田駿河台 1–8–11 東京YWCA会館 207 号室
製作：ジェイピーシー 144–0054 東京都大田区新蒲田 2–4–3 スポーツプラザビル401 Tel.（03）6715–7915
広告取扱い：科学技術社 111–0052 東京都台東区柳橋 2–10–8 武田ビル4F Tel.（03）5809–1132